

Originally published in *Proceedings of the Fifth International Workshop on Compressible Turbulent Mixing*, ed. R. Young, J. Glimm & B. Boston. ISBN 9810229100, World Scientific (1996).

Reproduced with the permission of the publisher.

Hydrodynamic Instability Experiments and Simulations*

Guy Dimonte, Marilyn Schneider,
C. Eric Frerking

Lawrence Livermore National Lab
Livermore, California 94551

Abstract. Richtmyer-Meshkov experiments are conducted on the Nova laser with strong radiatively driven shocks ($\text{Mach} > 20$) in planar, two-fluid targets with Atwood number $A < 0$. Single mode interfacial perturbations are used to test linear theory, and 3D random perturbations are used to study turbulent mixing. Rayleigh-Taylor experiments are conducted on a new facility called the Linear Electric Motor (LEM) in which macroscopic fluids are accelerated electro-magnetically with arbitrary acceleration profiles. The initial experiments are described. Hydrodynamic simulations in 2D are in reasonable agreement with the experiments, but these studies show that simulations in 3D with good radiation transport and equation of state are needed.

1 Introduction

The Richtmyer-Meshkov (RM) [1, 2] and Rayleigh-Taylor (RT) [3] instabilities occur when fluids of different densities are accelerated. In the RM instability, the acceleration is impulsive from a shock, and the fluid compression is important. In the RT instability, the acceleration is sustained but will vary in time in applications like inertial confinement fusion [4]. We investigate both instabilities using different experimental facilities and simulations using a Lagrangian-Eulerian code, CALE [5].

The RM experiments [6, 7, 8] are performed on the Nova laser at LLNL where pressures exceeding 30 Mb are obtained with a radiation drive. This extends previous investigations in shock tubes [2, 9, 10] to very high compression. We also use experimental techniques that avoid membranes and edge effects that have plagued shock tube experiments [11]. Experiments are conducted with single sinusoidal perturbations at the

*We thank the many talented people that have contributed to this work. This work was performed under the auspices of the U. S. Department of Energy by the Lawrence Livermore National Laboratory under Contract No. W-7405-END-48.

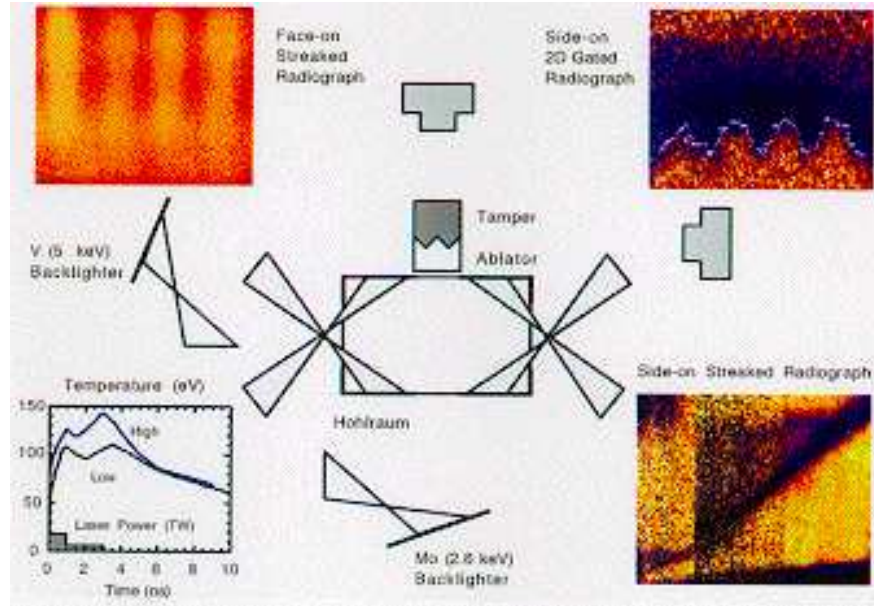


Figure 1: Experimental configuration and sample data.

interface to test linear theory. We find that the linear growth rates agree with a model suggested by Meyer and Blewett [12]. We also studied compressible turbulent mix with 3D random interfacial perturbations. The mix width is found to increase in time as $h \sim t^\beta$ with $\beta \sim 0.6 \pm 0.1$. Hydrodynamic simulations in 2D with a Lagrangian-Eulerian code [5] obtain comparable amplitudes, but the exponent is larger, $\beta \sim 0.9$.

The RT instability is investigated using a linear electric motor (LEM) to accelerate macroscopic fluids similar to the “rocket rig” experiments [13]. The acceleration is electro-magnetic so that the temporal shape is adjustable to generalize the mix scaling laws [13]. We obtain a constant acceleration $\sim 70g_0$ (earth’s gravity) or an impulsive acceleration with a peak $\sim 700g_0$. The initial results are reported here.

2 RM Experiments on Nova

The Nova experimental configuration has been described previously [6, 7, 8] and is shown in Figure 1. In order to produce a spatially uniform drive, eight laser beams (28 kJ at $0.53\mu\text{m}$) are converted to soft x-rays inside a cylindrical radiation enclosure called a hohlraum ($\sim 2-3$ mm diameter, 3–4 mm length). A 3 ns laser pulse generates a quasi-Planckian x-ray drive with a peak radiation temperature of ~ 140 eV. A HIGH and LOW drive is used in our experiments with different size hohlraums. The target

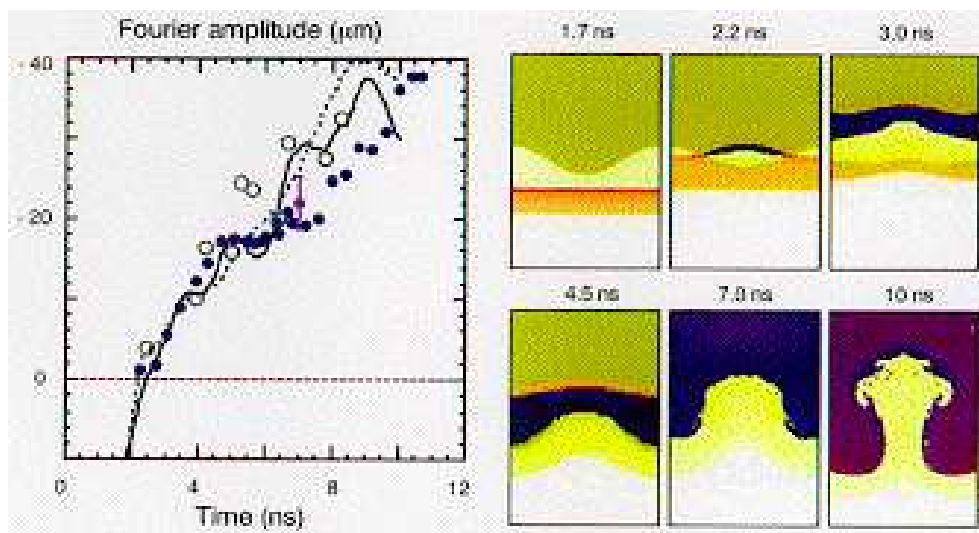


Figure 2: Fourier amplitude vs. time and CALE side-on images.

is mounted on the hohlraum wall and radiographed in-flight from the side and face-on using x-rays generated by two independent laser beams. A gated x-ray imager (GXI) obtains 2D radiographs and an x-ray streak camera obtains 1D images streaked in time.

The target consists of a beryllium (Be) ablator with density $\rho_1 = 1.7\text{g/cm}^3$ and a foam tamper with density $\rho_2 = 0.12\text{g/cm}^3$. The Atwood number is $A = (\rho_2 - \rho_1)/(\rho_2 + \rho_1) \sim 0.86$. The shock originates in the ablator and couples to the tamper while exciting perturbations imposed at the ablator/tamper interface. The shock characteristics (speed and compression) are obtained from streaked side-on radiographs as shown in Figure 1 taken with a smooth interface. For the single mode instability experiments, the perturbations are 2D, and the foam is opaque while the Be ablator is transparent. The growth of the perturbations is observed directly with 2D gated radiographs while a continuous record in time is obtained with streaked face-on radiographs. Examples of both are shown in Figure 1.

Figure 2 shows the temporal evolution of the imposed mode and images from the CALE simulation for a HIGH drive case. The initial perturbation has a wavelength of $\lambda = 100\mu\text{m}$ and an amplitude of $\eta_0 = 10\mu\text{m}$. The points are experimental: solid from face-on radiography and open from side-on radiography. The lines are from the simulations: solid from simulated face-on radiography and dashed from simulated side-on images. The experiment and simulation are in reasonable agreement. The perturbations invert when the shock traverses the interface near $t_i \sim 2\text{ ns}$ because $A < 0$. They then grow at an initial rate of $d\eta/dt \sim -8\mu\text{m/ns}$. At large amplitude, the growth rate

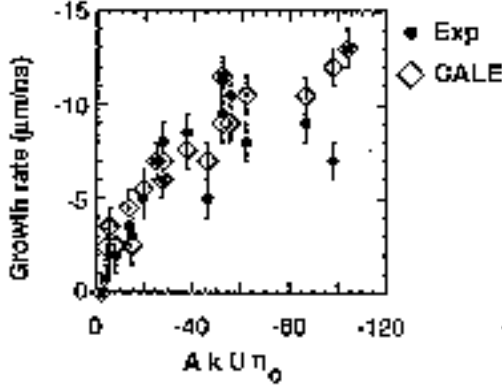


Figure 3: Growth rate vs. model parameter.

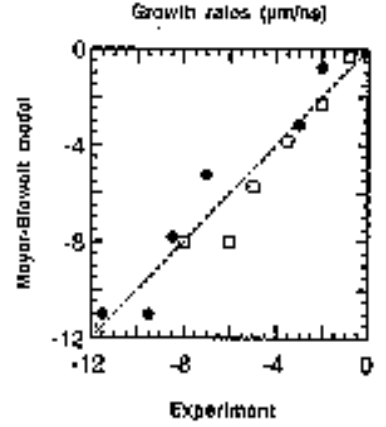


Figure 4: Meyer-Blewett vs. experimental growth rates.

declines as observed in previous experiments and simulations [14, 15]. The simulation images show the phase inversion, shock modulation and eventual nonlinear distortion of the perturbation.

The linear growth rate of the RM instability was obtained by solving the linearized fluid equations numerically for $A > 0$. As a result, Richtmyer [1] proposed the model

$$\frac{d\eta}{dt} = A^*kU\eta_0^* \quad (1)$$

where η is the amplitude, $k = 2\pi/\lambda$ and U is the shock induced interface speed. The post-shock values of A and η_0 (denoted by asterisks) are used to describe compressive effects. Meyer and Blewett performed full hydrodynamic simulations for $A > 0$ in agreement with Eq. 1. However, for $A < 0$, they obtained different growth rates and suggested the model

$$\frac{d\eta}{dt} = A^*kU(\eta_0 + \eta_0^*)/2 \quad (2)$$

For the conditions in Figure 2, we obtain $d\eta/dt \sim +11\mu\text{m}/\text{ns}$ from Eq. 1 and $d\eta/dt \sim -8\mu\text{m}/\text{ns}$ from Eq. 2. Please note that Eq. 2 agrees with our measurements and simulations whereas Eq. 1 disagrees in magnitude and sign because $\eta_0^* < 0$ with our high compression.

We compare the experimental and simulation growth rates over a wide range of conditions in Figure 3 by plotting them versus the figure of merit implied by Eqs. 1 and 2. For small values of $AkU\eta_0$, the growth rate increases with $AkU\eta_0$ consistent with the models. For large values, the growth rate approaches a limiting value perhaps due to

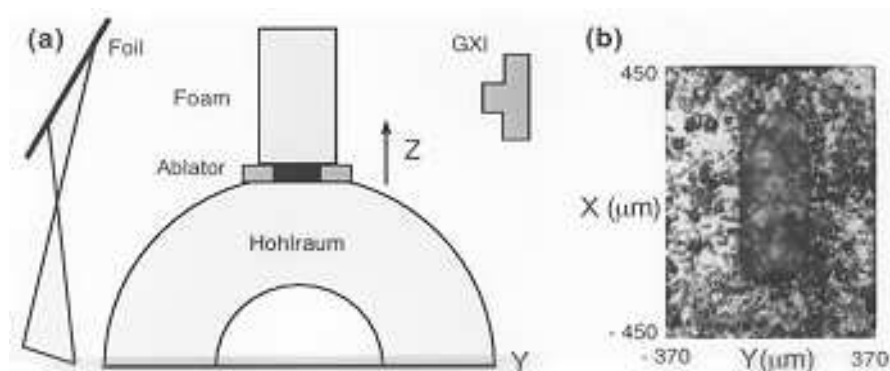


Figure 5: (a) Configuration and (b) ablator for turbulence experiments.

nonlinearities. We believe the limiting value is the difference between the transmitted shock speed V_2 and the interface speed, namely $d\eta/dt < V_2 - U \sim 20\mu\text{m/ns}$. This suggests that the tip of the perturbation must remain behind the transmitted shock. This seems reasonable because the perturbation spike would experience enhanced drag if it tried to penetrate the stationary upstream material.

We compare the measured growth rates with Eq. 2 in Figure 4 for the data subset with small initial amplitude $k\eta_0 < 1$. The agreement is very good. On the other hand, Eq. 1 predicts positive growth rates. These results indicate that a different expression for the growth rate is needed depending on the sign of A .

Turbulent mix is investigated by replacing the single mode interfacial perturbations with 3D random perturbations. In order to facilitate radiographic diagnosis, we modified the target because the interface can tilt or become bowed late in time and this can confuse the diagnosis. The configuration for these experiments is shown in Figure 5. The hohlraum geometry is similar to Figure 1, but the ablator is different as indicated by the photograph of the interface in Figure 5b. The ablator is still beryllium, but with a $250\mu\text{m}$ wide rectangular hole in the center which is filled with a Halar plastic ($\text{C}_4\text{H}_4\text{F}_3\text{Cl}$). Halar has a density of 1.68 g/cc , which is similar to beryllium, but contrary to Be, it is opaque to diagnostic x-rays. Thus, side-on radiographs sample only the central region of the target where the tilt and curvature are minimal and the turbulent mixing zone can be obtained from x-ray transmission profiles. Further details are described in [8]. The imposed interfacial perturbations are 3D, random and have a root-mean-squared amplitude of $\eta_{\text{rms}} \sim 4.6\mu\text{m}$ and a peak-to-valley amplitude of $h \sim 16\mu\text{m}$.

The shock induced motion is obtained from side-on radiographs as shown in Fig-

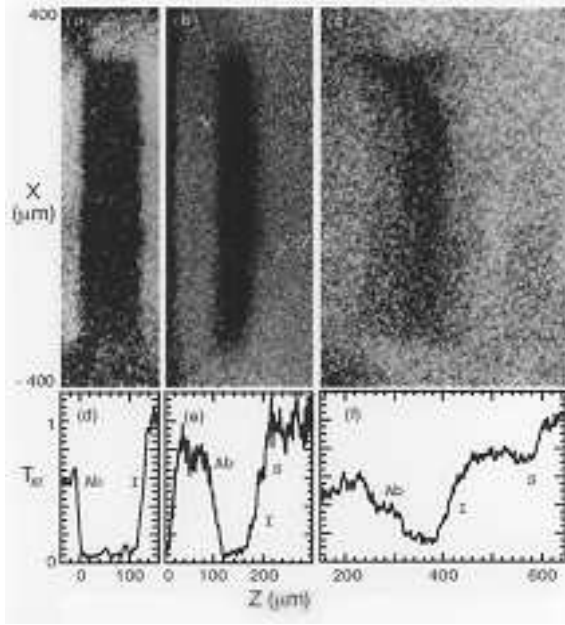


Figure 6: Nova experiment.

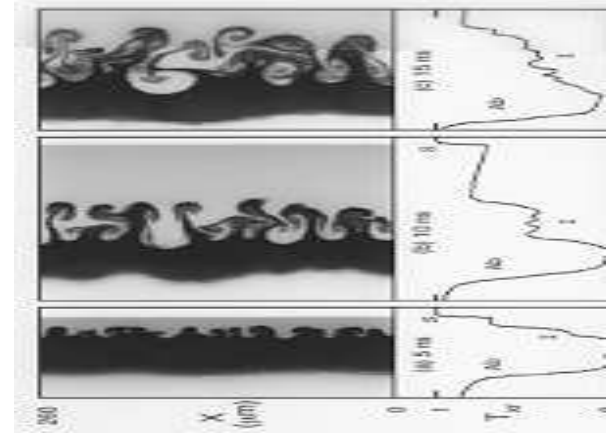


Figure 7: CALE simulation.

ure 6a-c at $t = 0, 4.7,$ and 10.2 ns. The radiographs are analyzed using the respective x-ray transmission profiles $T_{xr}(z)$ in Figure 6d-f, which are taken near $x = 0$ to minimize curvature effects and averaged over $\delta x \sim 150\mu\text{m}$ to reduce noise. The minimum in $T_{xr}(z)$ is $\sim 5\%$, rather than the expected 0.7% for Halar due to noise. However, the ablation front (Ab), interface (I), and shock (S) are discernible. At $t = 0$, the target is free standing to exhibit the ablation front. At $t = 4.7$ ns, the target is compressed and the transmitted shock is just ahead of the interface. At 10.2 ns, the transmitted shock is well ahead of the interface, and the shocked foam has $T_{xr} \sim 0.6$ as expected. The interface and ablation front broaden in time. Although it is difficult to see in Figure 6c, the shock develops an $850\mu\text{m}$ radius of curvature by 10.2 ns, which translates to an apparent width of only $\delta z \sim 9\mu\text{m}$ over the central $\delta x \pm 125\mu\text{m}$. From many measurements, we find that the incident shock reaches the interface ($z = 120\mu\text{m}$) at $t_i \sim 3.5 - 4$ ns, the transmitted shock has a velocity $V_2 \sim 70\mu\text{m}/\text{ns}$, and the shock induced interface speed is $U \sim 46\mu\text{m}/\text{ns}$. From the axial compression in the radiographs, we estimate a post-shock density of $\rho_1^* \sim 2\text{g}/\text{cm}^3$ for the ablator and $\rho_2^* \sim 0.35\text{g}/\text{cm}^3$ for the tamper. The post-shock Atwood number is $A^* \sim -0.7$.

The perturbation amplitude is determined from the gradient of the x-ray transmission profiles at the interface. The peak-to-valley interfacial mixing zone is identified as $h \sim \Delta T_{xr} (dT_{xr}/dz)^{-1}$, where ΔT_{xr} and dT_{xr}/dz are the jump and gradient in the

x-ray transmission at the interface, respectively. The technique is evaluated in-situ by radiographing a $50\mu\text{m}$ diameter tungsten wire and targets with known perturbations. The wire ($\tau \sim 50$) produces a minimum transmission of 5% ($\Delta T_{xr} \sim 95\%$) which is larger than expected and represents a noise baseline. In addition, the gradient length at the wire edge is $h \sim 10 - 12\mu\text{m}$ which is consistent with the GXI resolution. The initial profile in Figure 6d has a width of $h_{\text{exp}} \sim 19\mu\text{m}$ at the interface where $h_0 \sim 16\mu\text{m}$ and a smaller $h_{\text{exp}} \sim 13\mu\text{m}$ at the ablation front where $h_0 \sim 1 - 2\mu\text{m}$. We remove the systematic instrumental broadening by subtracting the GXI pinhole diameter $d = 10\mu\text{m}$ in quadrature from the measured value h_{exp} . This yields $h \sim 16\mu\text{m}$ at the interface in agreement with profilometry, but it still overestimates the width of the ablation front by $\sim 8\mu\text{m}$. This is a reasonable error estimate based on target tilt, curvature, and motion blurring. The profiles at 4.7 and 10.2 ns indicate a turbulent mix width of $h \sim 21$ and $75\mu\text{m}$, respectively.

The experiments are compared with 2D hydrodynamic simulations using the Lagrangian–Eulerian code CALE, which is driven with the measured radiation temperature profile. The equations of state for Be and Halar are approximated by B_4C with density $\rho_1 = 1.65\text{g/cm}^3$, and the foam is represented by CH with $\rho_2 \sim 0.12\text{g/cm}^3$. CALE obtains a peak pressure of 20 Mbar and average velocities $U \sim 46\mu\text{m/ns}$ and $V_2 \sim 70\mu\text{m/ns}$ similar to those measured. The incident shock velocity is $V_1 \sim 35\mu\text{m/ns}$ which has not yet been measured. Simulated side-on radiographs and associated transmission profiles are shown in Figure 7. The mix width increases to $h \sim 23, 82,$ and $113\mu\text{m}$ at 5, 10, and 15 ns, respectively. Although it is qualitative, bubble merger [13] is evident as the number of prominent features (amplitude $> 0.7h$) declines from 12 to 8 to 4 in time. The ablation front is also distorted mainly at long wavelength. The transmission profiles are monotonic at the interface similar to those measured except for the plateau at 10 ns. This is not seen experimentally because the perturbations are 3D, and the x-rays propagate through an ensemble of spikes.

Figure 8 shows the evolution of h for driven targets with $\eta_{\text{rms}} \sim 4.6\mu\text{m}$. The points are experimental with the instrumental correction and the solid line is from 2D CALE simulations. The perturbations are compressed with a phase reversal ($A < 0$) as the shock traverses the interface between $t_i \sim 3$ to 4 ns. The mix width then grown with comparable magnitudes in the experiment and simulations but at slightly different rates. To test self-similarity, we fit the power law $h \sim (t - t_i)^\beta$ to the experimental data and obtain $\beta \sim 0.6 \pm 0.1$. This agrees with the calculations [16] where $\beta \sim 0.4$ for bubbles and $\beta \sim 0.6$ for spikes at $|A^*| = 0.7$ (if they are symmetric in A^* since only $0 < A^* < 1$ was considered). The CALE growth rate is nearly constant for $t < 10$ ns and then declines, implying an effective $\beta < 1$. This discrepancy may be due to small scale resolution limitations or that CALE is 2D instead of 3D. Clearly, further developments in simulations are required.

The dashed line is obtained by assuming that the peak in the turbulent wavenumber

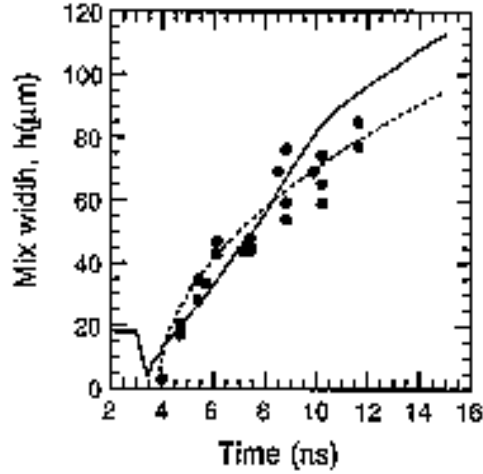


Figure 8: Mix width vs. time from experiment (points), CALE simulation (solid line), and dynamic scale model (dashed line).

spectrum evolves in time as the amplitude increases such that $\langle kh \rangle \sim \text{constant}$. By applying this dynamic scale approximation to Eq. 2, we obtain a mix width that increases as $h \sim (t - t_i)^{0.5}$ consistent with the measurements. These experiments extend shock tube experiments [17] to stronger shocks and indicate the need for 3D simulations [18].

3 RT experiments on the LEM

The Nova experiments are unique because they utilize a radiation drive to generate very strong shocks and high compression. However, the targets are small and turbulence is difficult to characterize over a wide range of spatial scales. Thus, we built a linear electric motor (LEM) to accelerate large fluids for diagnostic clarity and with an arbitrary acceleration profile. The configuration is shown in Figure 9 and described in [19].

The LEM consists of linear electrodes that conduct current through a sliding armature. This current and that flowing through an augmentation coil produce a magnetic field as shown in Figure 9. The product of the rail current and the magnetic field produces a downward force that can be programmed by varying the two current pulse shapes. The power is supplied by 16 independent circuits from an electrolytic capacitor bank with a total of 5.6 farad at 450 volt. Photographs of the LEM are shown

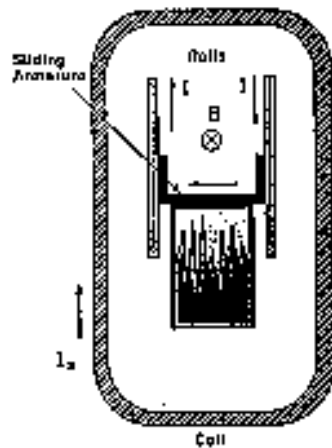


Figure 9: LEM configuration.

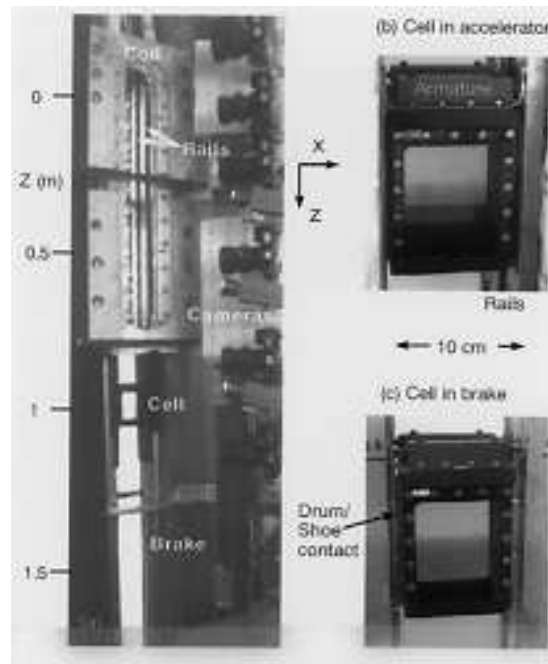


Figure 10: LEM photographs.

in Figure 10 with a long augmentation coil and a mechanical brake. The fluid cell is placed below the armatures as seen in Figure 10b in the accelerator and in the brake in Figure 10c. The cell has a total mass of ~ 2 kg and typical fluid dimensions of ~ 10 cm.

Two representative acceleration profiles are shown in Figure 11. A constant profile with $g \sim 70g_0$ is obtained for ~ 45 ms with 12 and 20 kamps in the rail and coil circuits, respectively. After 70 ms, the cell enters a mechanical brake which is open for diagnostic access. An impulsive profile with peak $g \sim 700g_0$ is obtained for 10 ms by increasing the rail and coil currents to 28 and 54 kamps, respectively. These profiles are designed to produce the same maximum velocity of ~ 30 m/s. Sample shadowgraphs are shown below each profile at the same displacement $z = 80$ cm for $A = 0.22$ (Freon/water). The turbulent mixing zone is the dark region in the center and clearly shows the importance of the acceleration profile. The dark region at the bottom of the impulsively accelerated case is due to cavitation in the Freon because the pressure drop across the Freon exceeds 15 psi for $g > 150g_0$.

References

- [1] R. D. Richtmyer, *Commun. Pure. Appl. Math.*, **13**, 297 (1960).

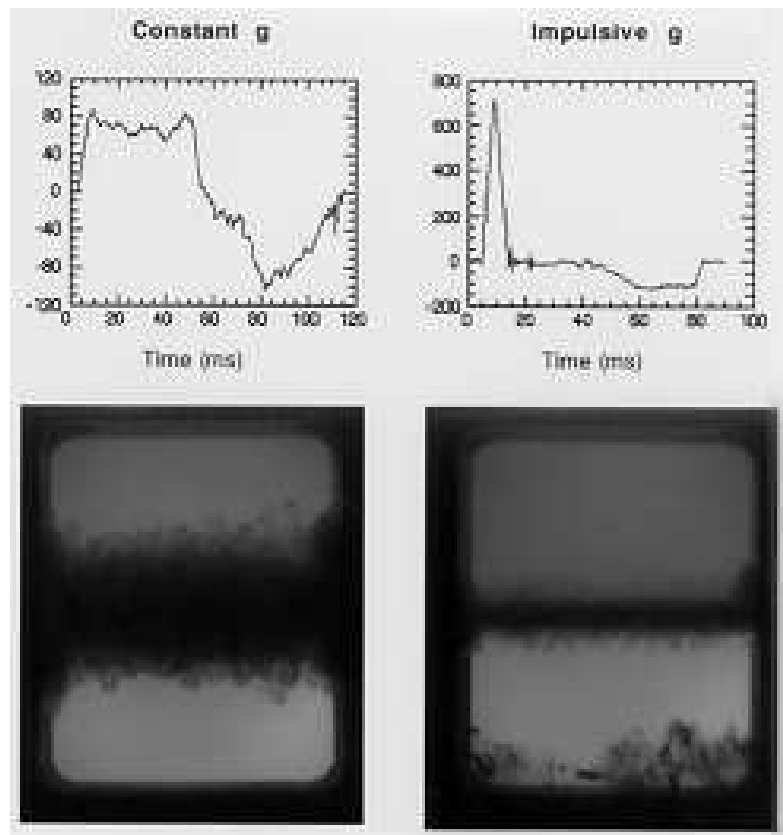


Figure 11: Acceleration profile and shadowgraph for constant and impulsive cases.

- [2] E. E. Meshkov, *Izv. Akad. Nauk SSSR Mekh. Zhidk. Gaza* **4** 151 (1969) [*Izv. Acad. Sci. USSR Fluid Dynamics* **4**, 101 (1969)].
- [3] Lord Rayleigh, *Scientific Papers II*, 200, Cambridge, England, 1900. Sir Geoffrey Taylor, *Proc. Roy. Soc. London* **A201**, 192 (1950).
- [4] J. D. Kilkenny et al., *Phys. Plasmas* **1**, 1379 (1994).
- [5] R. Tipton (private communication).
- [6] Guy Dimonte and Bruce Remington, *Phys. Rev. Lett.* **70**, 1806 (1993).
- [7] Guy Dimonte et al., (submitted to *Phys. Plasmas*).
- [8] Guy Dimonte, Eric Frerking, and Marilyn Schneider, *Phys. Rev. Lett.* **74**, 4855 (1995).
- [9] R. F. Benjamin, D. C. Besnard, and J. F. Haas, Los Alamos Report LA-UR 92-1185.
- [10] A. N. Aleshin et al., *Sov. Phys. Dokl.* **35**, 159 (1990).

- [11] M. Brouillette and B. Sturtevant, *J. Fluid Mech.* **263**, 271 (1994).
- [12] K. A. Mayer and P. J. Blewett, *Phys. Fluids* **15**, 753 (1972).
- [13] D. L. Youngs, *Physica D***12**, 21 (1984), K. I. Read, *Physica D***12**, 45 (1984).
- [14] L. D. Cloutman and M. F. Weiner, *Phys. Fluids A* **4**, 1821 (1992).
- [15] J. W. Grove, et al., *Phys. Rev. Lett.*, **71**, 3473 (1993).
- [16] U. Alon, et al., *Phys. Rev. Lett.* **74**, 534 (1995).
- [17] V. A. Andronov et al., *Sov. Phys. Dokl.* **27**, 393 (1982). S. G. Zaytsev et al., *Sov. Phys. Dokl.* **30**, 579 (1985).
- [18] D. L. Youngs, *Phys. Fluids A* **3**, 1312 (1991).
- [19] Guy Dimonte, et al., submitted to *Rev. Sci. Instruments*.